

Supporting Information

for

Nature of Peptide Wrapping onto Metal Nanoparticle Catalysts and Driving Forces for Size Control

Hadi Rezani-Dakhel,^{1,2,3} Nicholas M. Bedford,⁴ Taylor J. Woehl,⁴ Marc R. Knecht,⁵
Rajesh R. Naik,⁶ Hendrik Heinz^{1,7*}

¹ Department of Polymer Engineering, University of Akron, Akron, Ohio 44325, USA

² Institute for Molecular Engineering, University of Chicago, Chicago, Illinois 60637,
USA

³ Department of Biochemistry and Molecular Biology, University of Chicago, Chicago,
IL 60637, USA

⁴ Applied Chemicals and Materials Division, National Institute of Standards and
Technology, Boulder, Colorado 80305, USA

⁵ Department of Chemistry, University of Miami, Coral Gables, Florida 33146, USA

⁶ Materials and Manufacturing Directorate, Air Force Research Laboratory, Wright-
Patterson Air Force Base, Dayton, Ohio 45433, USA

⁷ Department of Chemical and Biological Engineering, University of Colorado-
Boulder, Boulder, Colorado 80309, USA

* Corresponding author: hendrik.heinz@colorado.edu

Table of Contents

Supporting Figures and Tables ... S3

Movie Caption ... S24

S1. Computational and Experimental Details ... S24

S2. Interpretation and Limitations of the Adsorption Index ... S42

S3. Additional Tests of Particle Size Using R→A Mutants ... S43

S4. Tests of Catalytic Activity ... S44

Supporting References ... S46

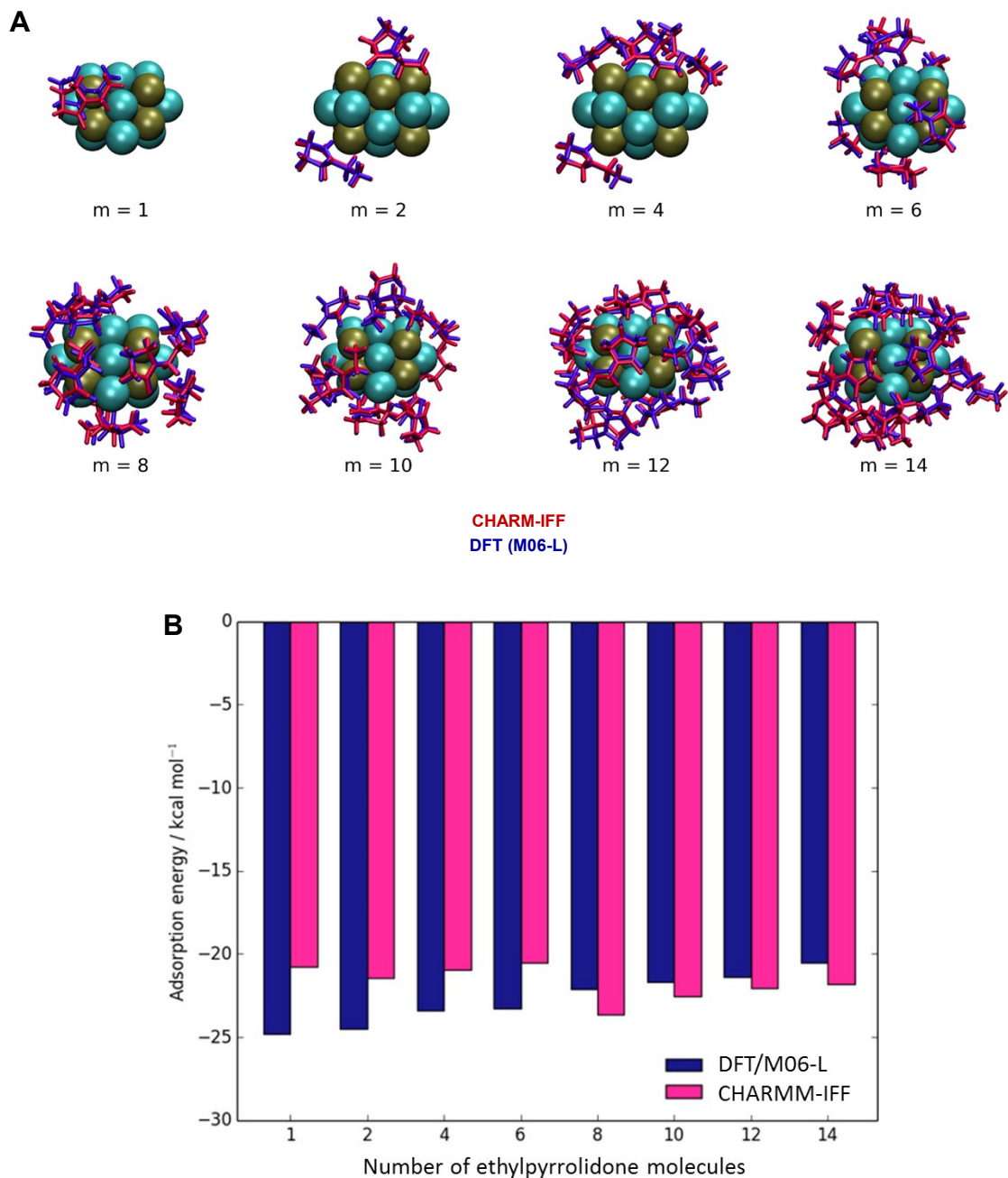


Figure S1. Validation of CHARMM-IFF in comparison to DFT (M06-L functional) for the adsorption of organic compounds onto small AuPd nanoclusters in vacuum according to ref. ¹. Small systems were chosen to be feasible for DFT calculations. (a) Optimized geometries of Au₁₀Pd₁₀ complexes with ethylpyrrolidone are compared and closely agree. *m* indicates the number of ethylpyrrolidone molecules. (b) Binding energies for all

complexes agree within 5-10%. The match is quantitative given that DFT is associated with uncertainties of at least 10% relative to experiment.

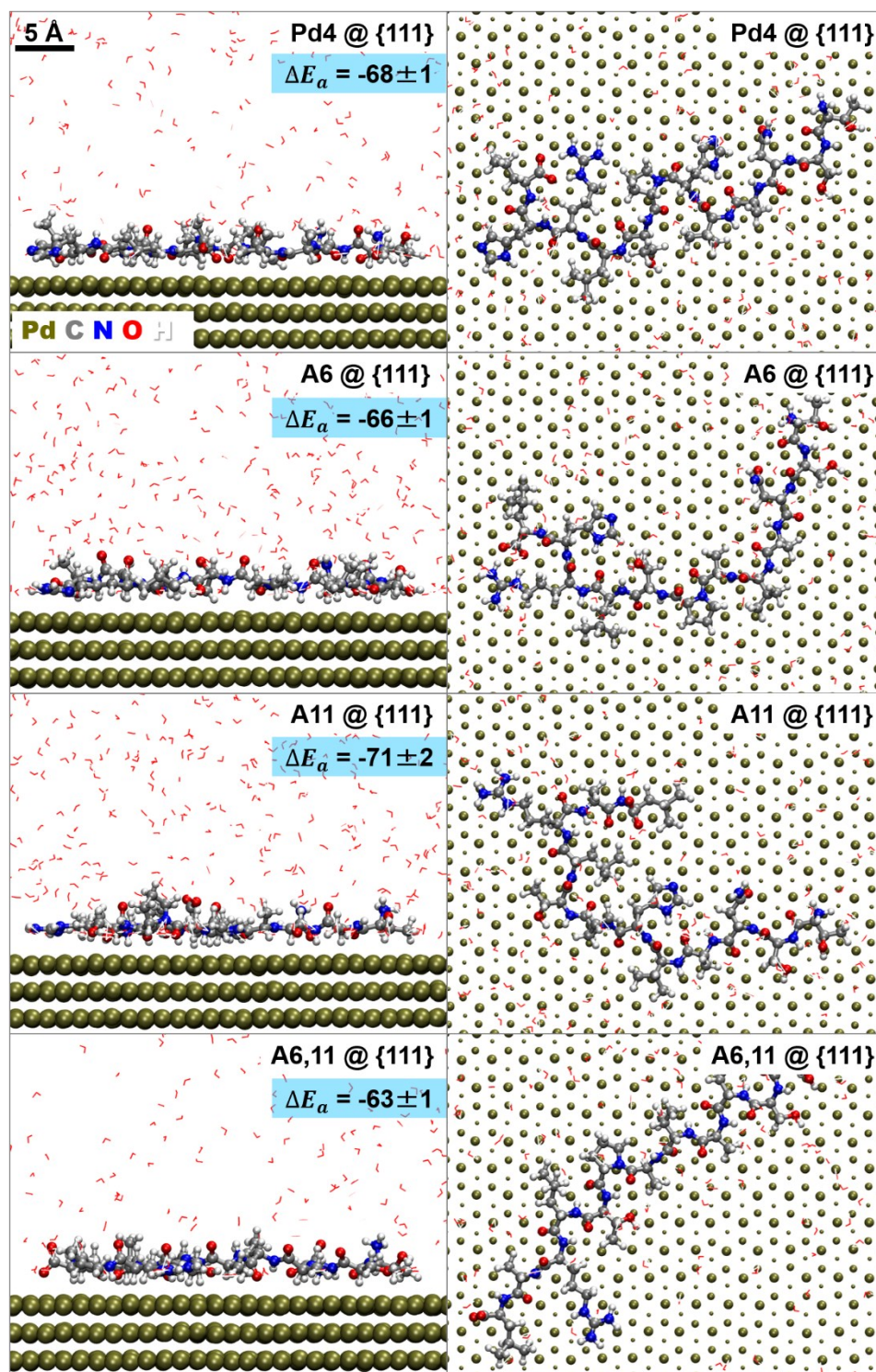


Figure S2. Conformations and adsorption energies of a single Pd4 peptide (TSNAVHPTLRHL) and its alanine mutants on flat palladium (111) surfaces in aqueous solution (surface coverage $\sim 30\%$). Soft epitaxial matching of polarizable atoms (C, N, O)

to the Pd surface can be seen, which includes the avoidance of metal atoms in the top layer (large spheres) and proximity to hollow sites in the two subsurface atomic layers (medium and small spheres). Extensive coordination of epitaxial sites causes very strong adsorption in the range -63 to -71 kcal/mol.

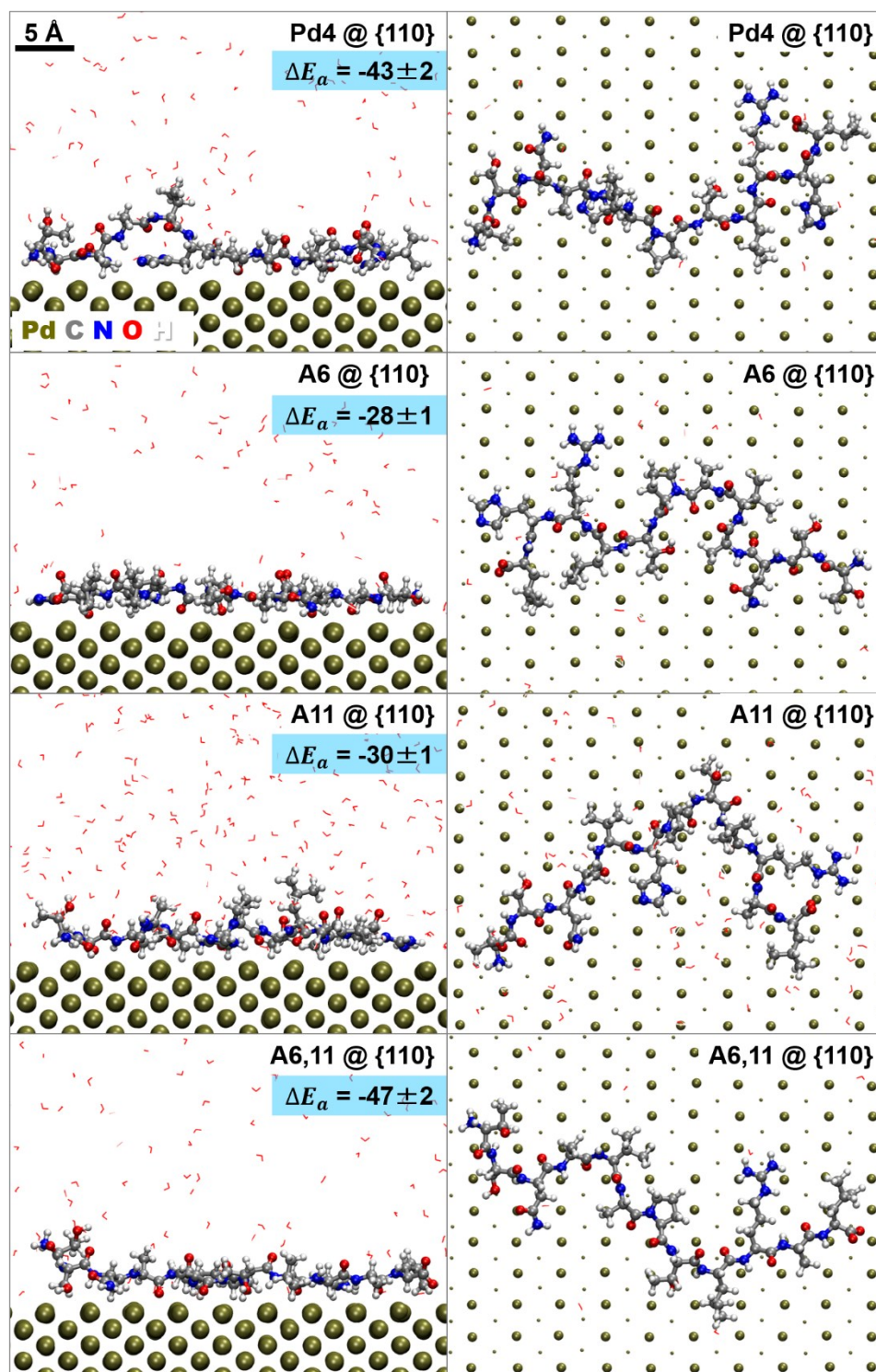


Figure S3. Conformations and adsorption energies of a single Pd4 peptide (TSNAVHPTLRHL) and its alanine mutants on flat palladium (110) surfaces in aqueous solution (surface coverage $\sim 30\%$). Soft epitaxial matching of polarizable atoms (C, N, O)

to the Pd surface can be seen, which involves the avoidance of surface atoms in the top layer (larger spheres) and proximity to hollow sites in the surface (smaller spheres). The characteristic, 3.9 Å wide vertical grooves accommodate several side chains. The wide grooves also lead to less specific epitaxial matching in comparison to the smaller hexagonal spacing of epitaxial sites of 1.59 Å on the (111) surface. The still high degree of epitaxial fit leads to strong adsorption energies in the range -28 to -47 kcal/mol.

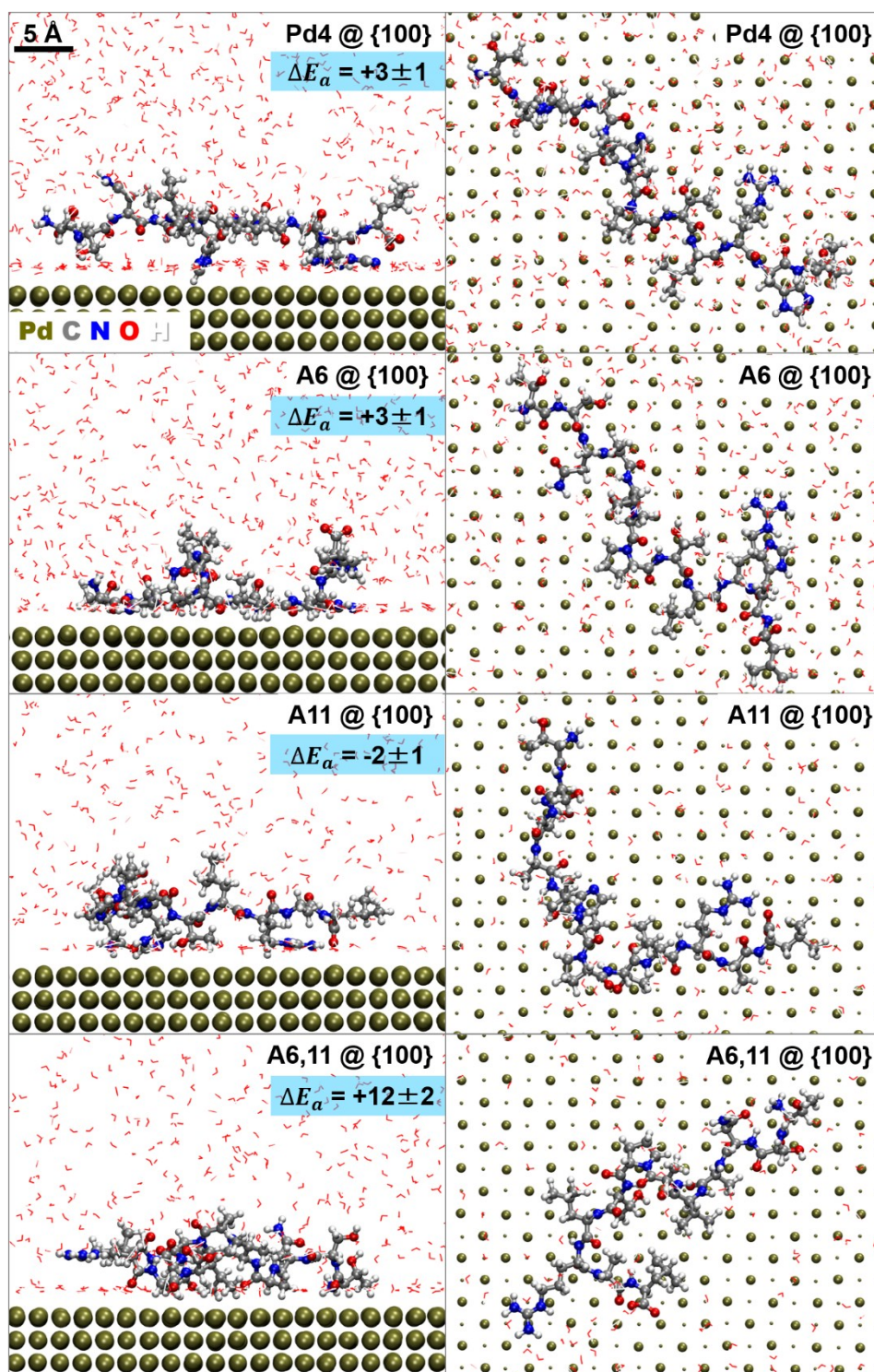


Figure S4. Conformations and adsorption energies of a single Pd4 peptide (TSNAVHPTLRHL) and its alanine mutants on flat palladium (100) surfaces in aqueous solution (surface coverage $\sim 30\%$). The peptides barely coordinate epitaxial sites due to the

large quadratic spacing of 2.75 Å. Most binding occurs through oxygen atoms in water that remain close to hollow sites in the subsurface atomic layer (smaller spheres) and avoid surface atoms in the top layer (larger spheres). The peptides are separated, or partially separated, from the metal surface by a water layer and binding energies range from -2 to +12 kcal/mol. Positive binding energies indicate desorption from the surface.

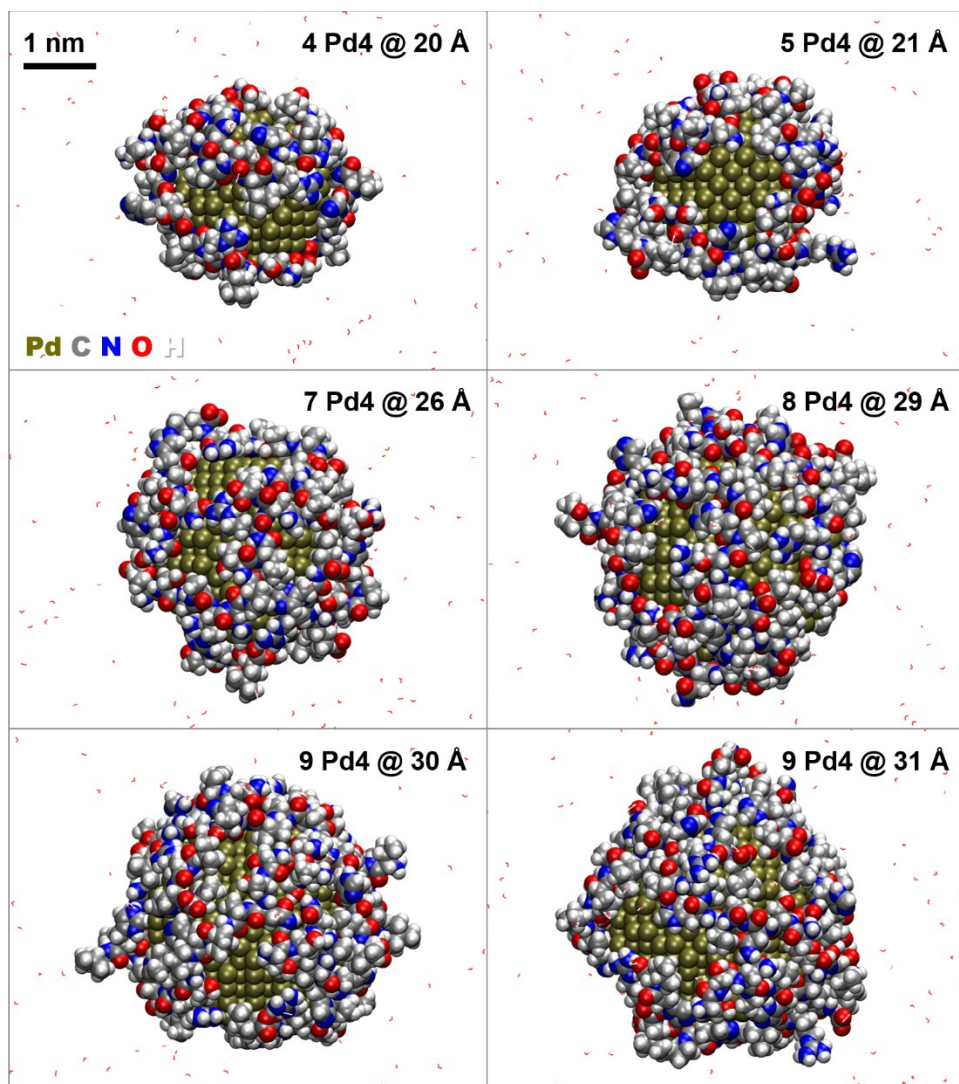


Figure S5. Equilibrium conformations of peptide Pd4 on palladium nanoparticles of different size in aqueous solution at monolayer surface coverage. The number of peptides per particle is 4, 5, 7, 8, 9, and 9, respectively.

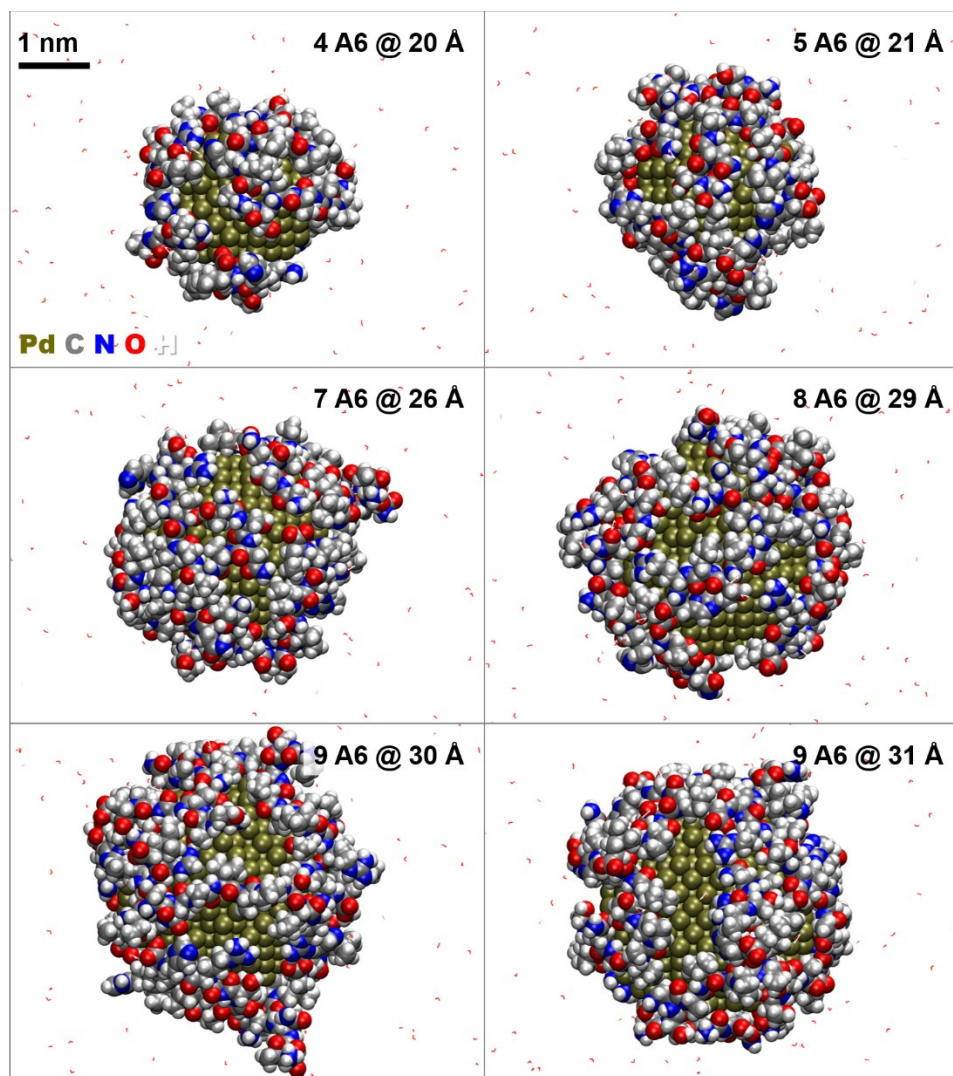


Figure S6. Equilibrium conformations of peptide A6 on palladium nanoparticles of different size in aqueous solution at monolayer surface coverage. The number of peptides per particle is 4, 5, 7, 8, 9, and 9, respectively.

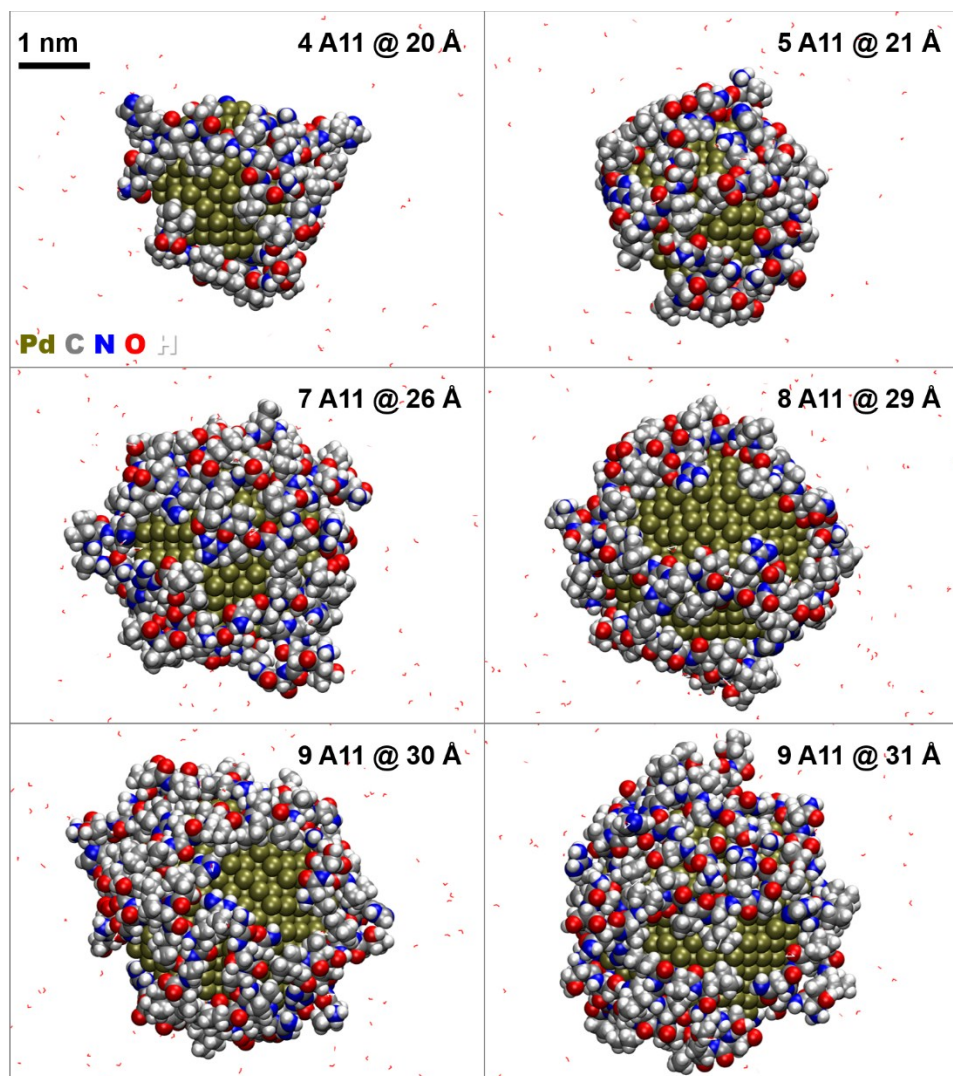


Figure S7. Equilibrium conformations of peptide A11 on palladium nanoparticles of different size in aqueous solution at monolayer surface coverage. The number of peptides per particle is 4, 5, 7, 8, 9, and 9, respectively.

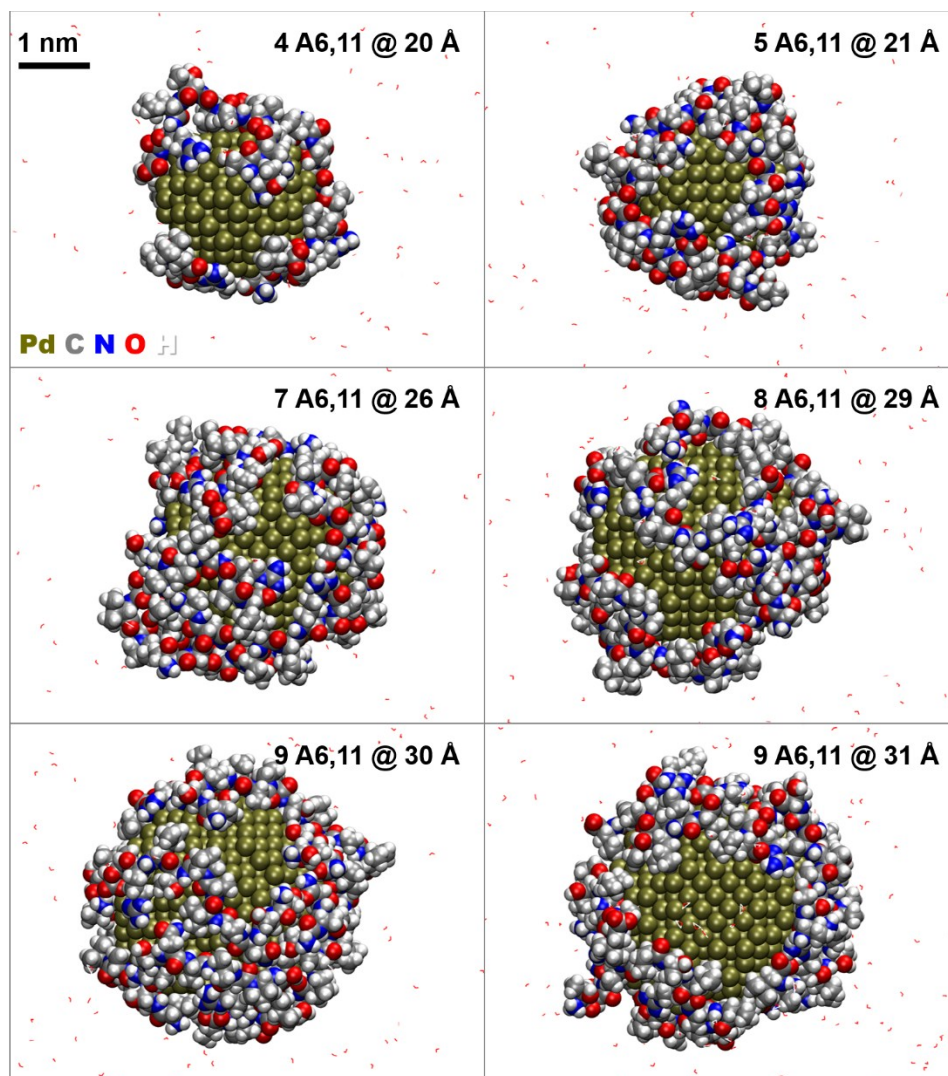


Figure S8. Equilibrium conformations of peptide A_{6,11} on palladium nanoparticles of different size in aqueous solution at monolayer surface coverage. The number of peptides per particle is 4, 5, 7, 8, 9, and 9, respectively.

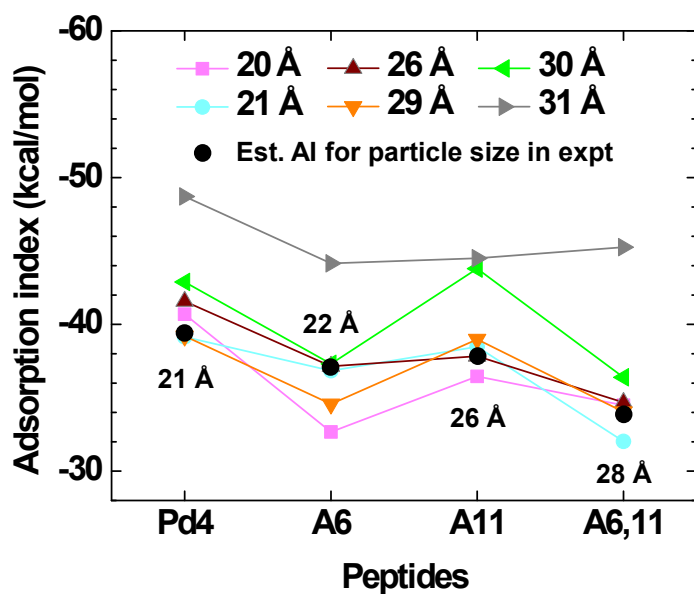


Figure S9. The adsorption index (AI) of peptides bound to nanoparticles of various size, including an estimate for the average particle size observed in experiment (black circles, 21, 22, 26, and 28 Å). The AI estimates adsorption energies of peptide monolayers onto Pd nanoparticles using known adsorption energies of single peptides on extended (hkl) surfaces and the (hkl) portions covered by the peptides. For a given peptide, adsorption tends to be stronger on larger nanoparticles. Larger observed particle size correlates with weaker adsorption index (closer to zero).

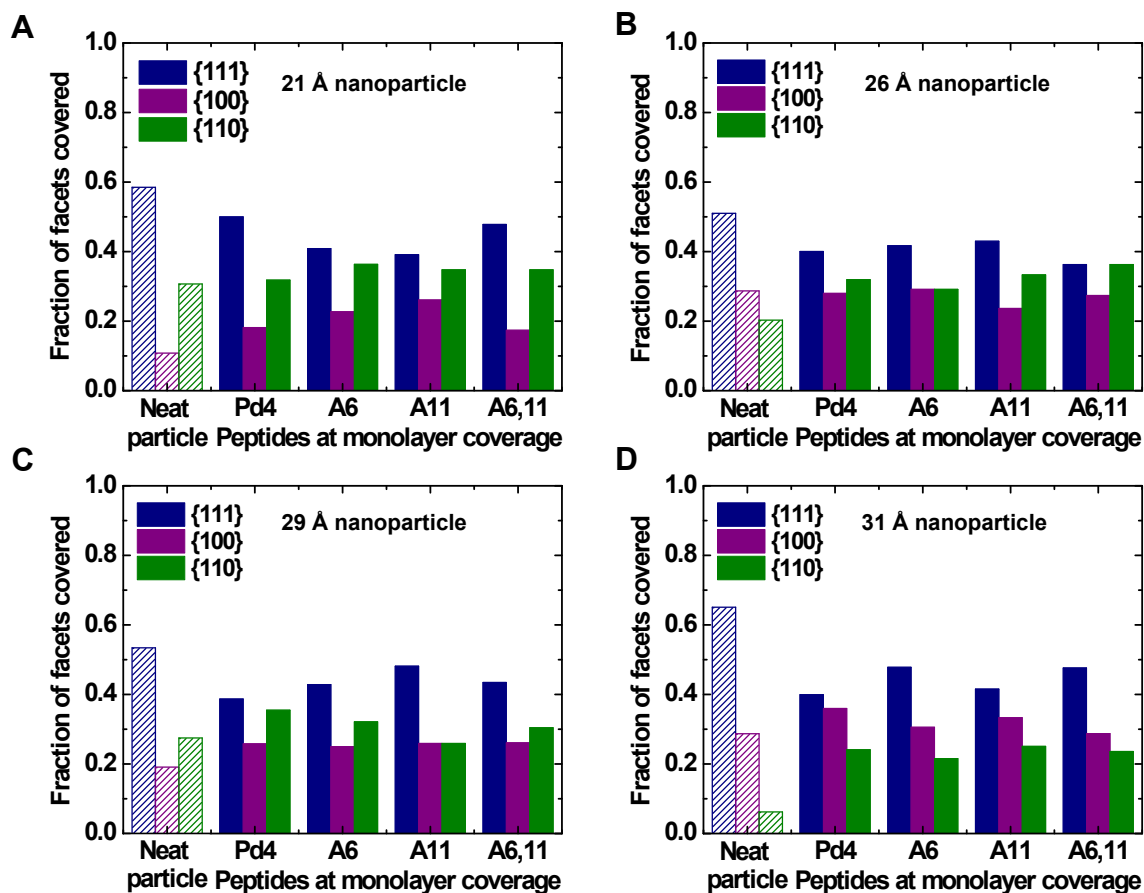


Figure S10. Facet coverage of different peptide backbones (Pd4, A6, A11, A6,11) on nanoparticles of different size at monolayer coverage in solution (pH 7). (a) 21 Å particle diameter. (b) 26 Å particle diameter. (c) 29 Å particle diameter. (d) 31 Å particle diameter. The facet composition of the bare, uncovered nanoparticles (patterned bars) approximately guides the adsorption of bound peptide backbones in aqueous solution (solid bars). A trend towards equalization of facet coverage as well as unique patterns of facet coverage due to mutations in the amino acid sequence are seen. (Note that side chains of the peptides are disregarded in this analysis for simplicity.)

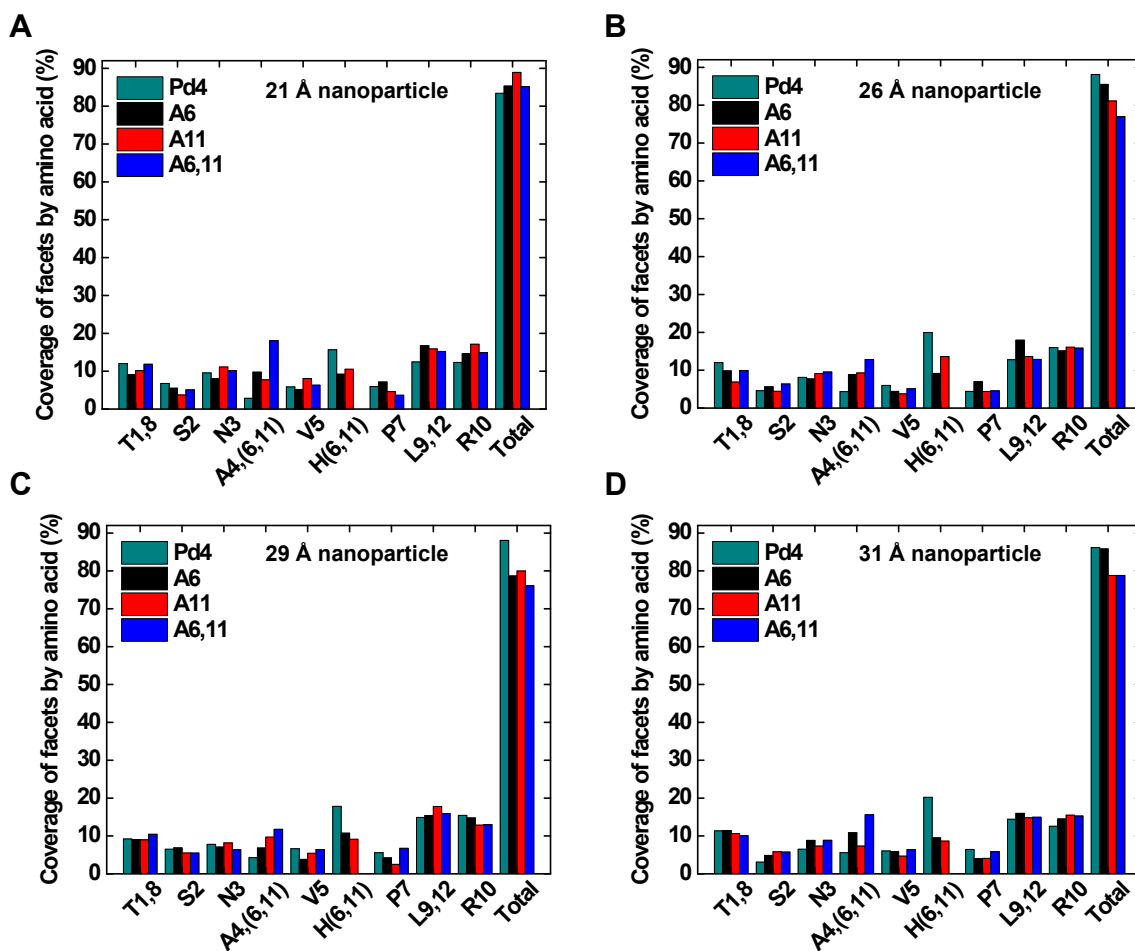


Figure S11. Breakdown of the contribution of individual amino acids to the overall surface coverage of the nanoparticles. The data are shown in groups of four columns for each of the different peptides. (a) 21 Å nanoparticle. (b) 26 Å nanoparticle. (c) 29 Å nanoparticle. (d) 31 Å nanoparticle. Arginine contributes most to the surface coverage (~15%). For amino acids that are present twice in a peptide (e.g., T1,8), the values in the bar chart represent the total for both residues. (Side chains of the peptides are included in this analysis).

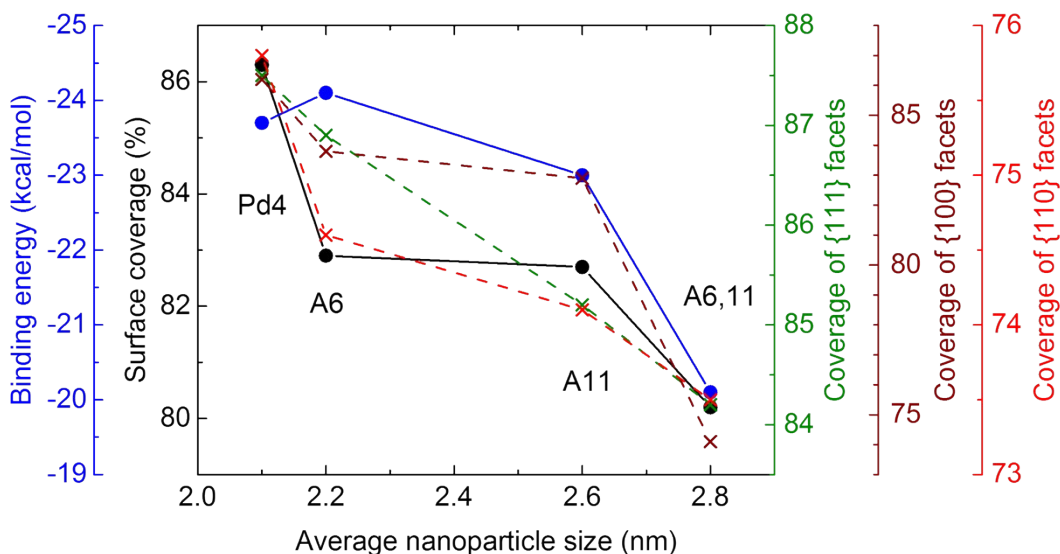


Figure S12. Summary of the relationship of average nanoparticle size in synthesis to the binding energy of the peptide (blue curve) and to the surface coverage (black curve). The relation between average particle size and surface coverage shows the same trend for the three individual facets (dotted curves). The binding energies and surface coverages are an average over all six nanoparticles for each peptide that leads to the given average particle size (Pd4 for 2.1 nm particles, A6 for 2.2 nm particles etc). The data correspond to binding energies of the peptides to nanoparticles in Figure 1b and data on surface coverage in Figure 3a. Error bars are omitted for clarity. The uncertainties are $\pm 1.0\%$ in surface coverage, ± 0.5 kcal/mol in binding energy, and about ± 0.1 nm in average particle size (from TEM), explaining some irregularity of the plot. The trends of each individual measure are significant and in the same direction.

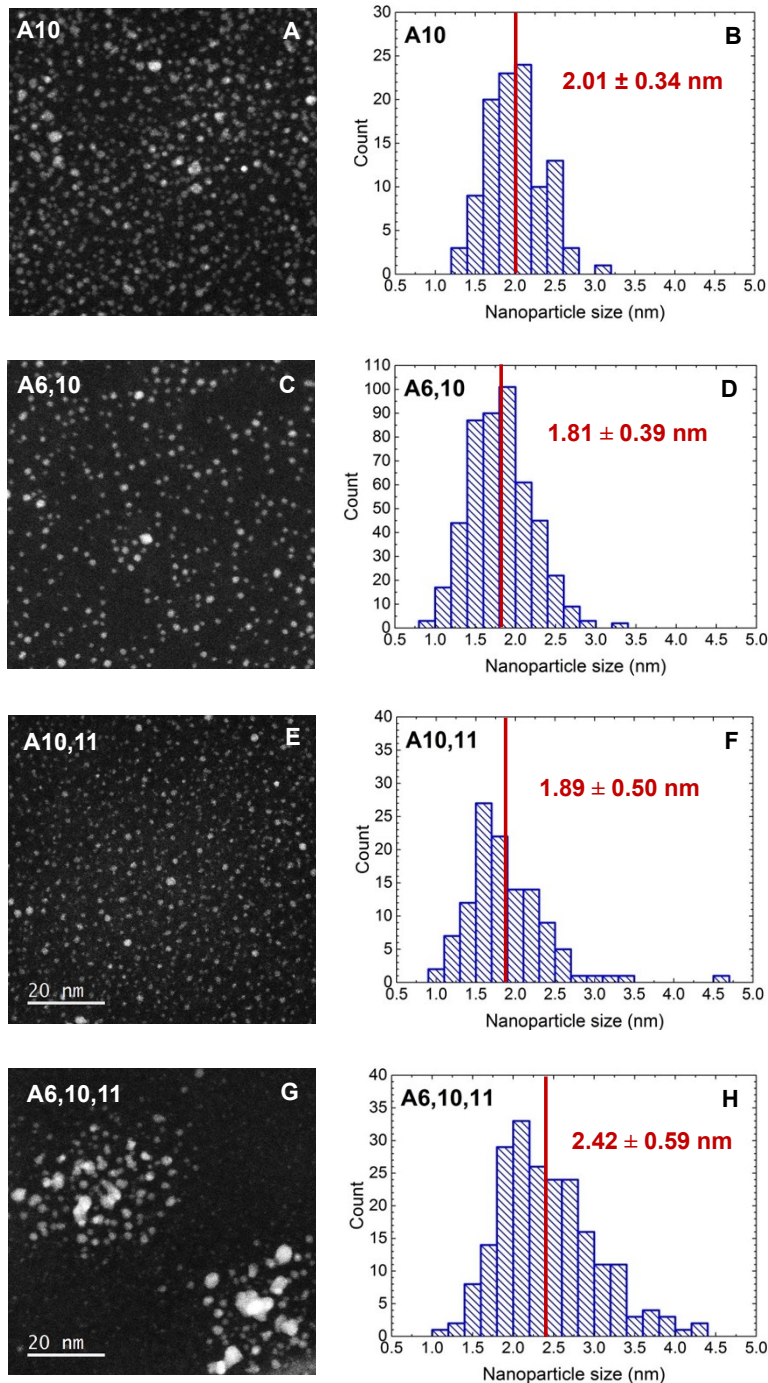


Figure S13. TEM images and histograms of the size distribution of Pd nanoparticles synthesized using arginine mutations of peptide Pd4 to (R10 to A10) during seed growth. (a, b) A10 peptide. (c, d) A6,10 peptide. (e, f) A10,11 peptide. (g, h) A6,10,11 peptide. Nanoparticles synthesized using A10 are smaller while A6,10 and A10,11 peptides show

a higher percentage of larger nanoparticles. The Pd nanoparticles from the A6,10,11 peptide exhibit several larger and agglomerated particles, indicating lower surface coverage on large nanoparticles and lower binding strength.

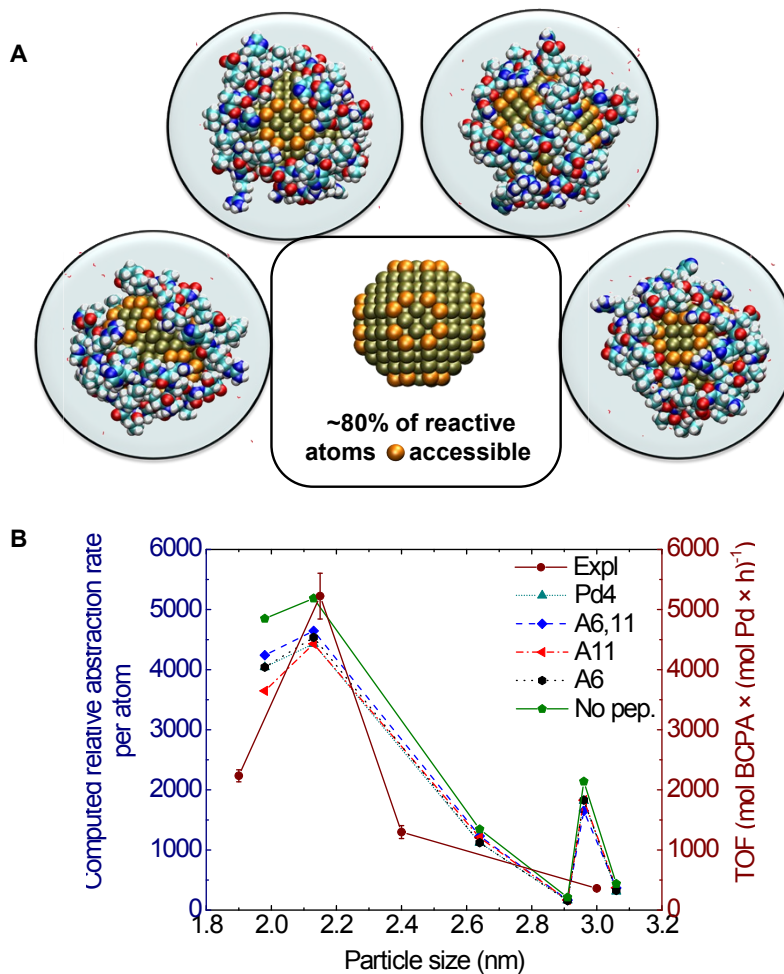


Figure S14. Influence of surface coverage with peptide on the catalytic activity of Pd nanoparticles in Stille coupling reactions and comparison of measured versus computed reaction rates (see details in ref. ²). (a) Four different views onto the 21 Å nanoparticle covered with Pd4 peptides at monolayer coverage. Approximately 80% of undercoordinated reactive surface atoms remain accessible (highlighted). (b) Correlation

of computed relative reaction rates of bare and peptide-covered Pd nanoparticles with experimentally measured turnover frequencies. Coverage with different peptides reduces the reaction rate similarly by ~20% so that relative reaction rates of given particles remain relatively unaffected by the presence of the ligands in Stille coupling reactions (note that ligands may play a major role in hydrogenation, for example).

Table S1. Peptide sequences including further R→A (red) mutants and the size of Pd nanoparticles derived in colloidal synthesis.

Peptide name	Peptide sequence	Particle size (nm)
Pd4	TSNAVHPTLRHL	2.1 ± 0.4
A6	TSNAV ^A PTLRHL	2.2 ± 0.7
A11	TSNAVHPTLR ^A L	2.6 ± 0.4
A6,11	TSNAV ^A PTLR ^A L	2.8 ± 0.7
A10	TSNAVHPTL ^A H ^L	2.0 ± 0.3
A6,10	TSNAV ^A PTL ^A H ^L	1.8 ± 0.4
A10,11	TSNAVHPTL ^A ^A L	1.9 ± 0.5
A6,10,11	TSNAV ^A PTL ^A ^A L	2.4 ± 0.6

Table S2. The number of atoms in the atomistic models of stable Pd nanoparticles and the number of peptides to approximate monolayer coverage in molecular dynamics (MD) simulations.

Particle size (Å)	# of Pd atoms	# of peptides in MD
20	321	4
21	369	5
26	675	7
29	935	8
30	959	9
31	1055	9

Table S3. Approximate maximum surface area covered by each amino acid on a flat metal surface. Relative uncertainties on the basis of the visual analysis are $<\pm 0.5\%$. (The absolute uncertainty could be up to $\pm 5\%$ depending on the definition of maximum coverable surface area.)

Amino acid	Max. surface area (Å ²)
THR (T)	26.0
SER (S)	24.0
ASN (N)	33.0
ALA (A)	20.0
VAL (V)	28.6
HIS (H)	36.0
PRO (P)	26.4
LEU (L)	30.8
ARG (R)	48.0

Movie S1. The movie shows an animation of the assembly of five Pd₄ peptides on a Pd nanoparticle (21 Å) in aqueous solution, and then illustrates the analysis of conformations and reactivity. Sections include (i) peptide assembly without water, (ii) the equilibrium trajectory of the peptides in contact with the nanoparticle in water, (iii) analysis of particle surface coverage by individual amino acids, and (iv) visualization of reactive atoms in Stille coupling and their accessibility through the ligand shell. Other particle/peptide combinations were analyzed analogously.

S1. Computational and Experimental Details

Extensive atomistic molecular dynamics simulations were carried out to compute binding configurations and adsorption energies of the Pd₄ peptide and three H→A mutant peptides on the extended low-energy surfaces of palladium, *i.e.*, (111), (110), and (100), as well as on six near-spherical Pd nanoparticles with sizes from 1.9 to 3.1 nm. All calculations were carried out in explicit water and included advanced sampling methods to obtain fully equilibrated structures of peptides on the surfaces. Subsequently, the wrapping geometry of the peptide backbone around the particles, the surface coverage by individual amino acids, binding energies, and relative reactivity of the nanoparticles in carbon-carbon coupling reactions (Stille coupling reactions) were analyzed. The construction of models, choice of force field, simulation protocols, analysis, and experimental details are described in the following. Parts of the simulation protocols, synthesis, and characterization have been applied previously and can be viewed in earlier publications for additional details.²⁻⁴

Experiments in this study involved the synthesis of new peptide sequences from the Pd₄ peptide with R→A substitutions, growth and characterization of nanoparticles derived

in the presence of these peptides (Table S1). Computational and experimental details are described in detail below.

S1.1. Construction of Molecular Models. The graphical user interfaces of Hyperchem⁵ and Materials Studio⁶ were employed to build all-atom models of the peptides Pd4, A6, A11, A611, and models of TIP3P water. The protonation state of the peptides was adjusted to represent neutral conditions as in experiment ($\text{pH} \simeq 7$). Accordingly, all peptides were represented in the zwitterionic state. The guanidinium group in arginine was protonated (positively charged) and the charge compensated by a chloride ion. All other residues and overall simulation boxes remained charge-neutral. The charge state of the Pd peptide and of the three H→A mutants may be represented as T(+) $\text{SNAV(H, A)PTLR(+)(H, A)L(-)} \cdot \text{Cl}^-$.

Four to six different initial conformations of each peptide including α -helix, β -sheet, β -turn, and random coils were prepared. Diverse peptide-surface orientations and peptide arrangements on the nanoparticle surfaces were chosen to construct initial models. This approach, along with effective sampling protocols, ensures inclusiveness of the energy landscape of peptides and peptide-surface orientations. Trapping of particular secondary structures and binding configurations in local energy minima, which would result in (inaccurate) higher adsorption energies, can be prevented for peptides of this length (12 amino acids or shorter).³

3D atomistic models of thermodynamically stable, idealized, near-spherical fcc nanocrystals were prepared following a prior protocol (Table S1).⁴ The models are not specifically matched to HE-XRD/PDF data. Specifically matched models to HE-XRD/PDF

data would represent realistic but less stable structures and were previously analyzed for accurate rate predictions.²

A summary of the protocol to construct models of stable near-spherical nanoparticles is as follows (see ref. ⁴): Model building started with a $8\times 8\times 8$ supercell of crystalline palladium using X-ray data of the unit cell.⁷ A central atom was selected and a spherical cutoff was applied to include palladium atoms within a spherical region. The cutoff radius was varied from 9 Å to create a particle of ~ 18 Å diameter and incremented in small steps of 0.1 Å to obtain every possible near-spherical particle size up to ~ 31 Å diameter. The raw particle models were subjected to molecular dynamics simulation using the CHARMM-INTERFACE force field, including annealing at elevated temperatures for several nanoseconds. The cohesive energies of the nanoparticles at room temperature were plotted as a function of particle size on a master curve to identify thermodynamically more stable nanoparticles and thermodynamically less stable nanoparticles.⁴ The six chosen nanoparticle models correspond to the most stable structures in the size range from 19 Å to 31 Å (Table S2). These particle models were used to analyze peptide wrapping, facet coverage, adsorption, and reactivity.

S1.2. Setup of Molecular Dynamics Simulations and Calculation of Adsorption Energies. The simulation of equilibrium conformations and adsorption energies of single peptides on the flat surfaces and of peptide monolayers on the nanoparticles involved four simulation boxes for each replica of a given peptide-particle combination. The boxes contained (1) particle-peptide-water, (2) peptide-water, (3) particle-water, and (4) pure water, respectively.⁸ The water portion consisted of 2000 water molecules in each box. The

total number of atoms in boxes (1) and (4) was the same as the total number of atoms in boxes (2) and (3). Adsorption energies were computed using the following equation:

$$E_{ads} = E_1 + E_4 - (E_2 + E_3) \quad (S1)$$

In the presence of multiple charged groups and ions, a two-box method that combines boxes (1) and (4), as well as boxes (2) and (3), is typically preferable since ions tend to diffuse across the entire box volume. Splitting of boxes can prevent sampling of the configuration space of charged moieties and introduce significant inaccuracy. In the present study, however, we found that the four-box method still yielded the same results as the two box method and reduced the already extensive computation time. Accordingly, E_4 was a constant value for all peptide-particle combinations, and E_3 only needed to be evaluated once for every particle in water.

The concentration of peptides in experiment is typically lower than the threshold concentration for self-assembly into sheets, agglomerates, and other superstructures (<200 $\mu\text{g/ml}$) so that peptide molecules in solution remain mostly isolated.^{2, 3, 9-13} To avoid very large simulation boxes with up to 9 peptides detached from the particle surface and lots of water molecules (Table S2), the energy of N non-interacting single peptides in solution E_2 was calculated using a multiple of the total energy of a single peptide dissolved in water E_{2S} , followed by subtraction of the energy of $(N - 1)$ boxes of pure water E_4 :

$$E_2 = NE_{2S} - (N - 1)E_4. \quad (S2)$$

In case $N = 1$, $E_2 = E_{2S}$. The computed adsorption energies E_{ads} according to equation (S1) were normalized per mol peptide, *i.e.*, the unit kcal/mol signifies “adsorption energy in kcal per mol peptide” throughout this work.

The peptide molecules were initially distributed around the particles in vacuum within 7 Å to 12 Å distance from the surface to allow free assembly on the particle surface (Movie S1). Following brief energy minimization (100 steps), 1 ns molecular dynamics simulation in the NVT ensemble at room temperature was carried out to allow initial assembly of the peptides on the particles. As a next step, pre-equilibrated stacks of water molecules were added to each individual system by superposition (~10 stacks of 200 water molecules). Minor overlaps and close-contacts between water molecules and peptides were eliminated through translational moves, energy minimization, and short molecular dynamics simulation with small time-steps (*e.g.* 0.1 fs) subsequently.

On the extended (hkl) surfaces of Pd, single peptides were initially placed close to the metal surface for each peptide-surface combination. Then, energy minimization was carried out followed by molecular dynamics and addition of water molecules. For some replicas, water molecules were added to the system at the same time as the peptides. Overlaps between water and peptide molecules were removed using translational moves, energy minimization, and short molecular dynamics simulation with small time-steps (*e.g.* 0.1 fs).

All four simulation boxes of a given particle-peptide-water combination including the pure-water, peptide-water, and surface-water systems were constructed five to six times with various initial surface-peptide orientations and different secondary structures of the peptides. The multiple replicas enhanced conformation sampling of slow conformation transitions and aid in the calculation of adsorption energies with good statistics and low uncertainty (± 1 to ± 2 kcal/mol).^{8, 14}

Details are also given in prior references.^{2, 3, 8, 10}

S1.3. Force Field. The CHARMM-INTERFACE force field (CHARMM-IFF) was used for accurate simulations of bulk properties and inorganic-organic interactions.^{15, 16} It includes the CHARMM27 parameters for the peptides¹⁷ and Lennard-Jones parameters for the fcc metals.¹⁸ The parameters predict the density and (hkl) surface energy energies of metals,¹⁸ facet-specific binding preferences,¹⁹ adsorption energies in quantitative agreement with experiment,^{14, 20} as well as shape preferences upon nanocrystal growth,^{3, 13} and reaction rates using reactive molecular dynamics.² Recently, binding energies of organic ligands to small metal nanoparticles were computed by CHARMM-IFF and shown to agree with DFT calculations within 10% deviation (Figure S1).¹ DFT methods may be in fact less reliable as they reproduce surface energies of metals with errors of 20-50%,²¹ i.e., one order of magnitude larger error than with CHARMM-IFF (0-5%).¹⁸ Reactive extensions of CHARMM-IFF for covalent adsorption of thiols and predictions of relative reaction rates in C-C coupling and hydrogenation reactions in very good accuracy have been demonstrated as well.^{2, 10, 11}

The INTERFACE force field is based on a classical Hamiltonian and compatible with the common energy expressions such as CHARMM, CVFF, AMBER, PCFF, GROMACS to cover compounds and inorganic/biological multiphase systems across the periodic table. Main characteristics are the chemically consistent representation of atomic charges to model the balance of covalent versus ionic bonding, the reproduction of structures, energies, and energy derivatives in excellent agreement with experiment.¹⁵ Fcc metals are represented by thermodynamically consistent Lennard-Jones (LJ) parameters.¹⁸ Polarizable LJ parameters have been recently introduced, however, changes in adsorption in aqueous solution are small and no external electric fields were applied in this study.

Interactions between different atom types such as Pd metal and peptides are described by standard combination rules. In CHARMM-IFF these are the Lorentz-Berthelot²² combination rules that involve an arithmetic average of σ ($\sigma_{ij} = \frac{\sigma_i + \sigma_j}{2}$) and a geometric mean of ε ($\varepsilon = \sqrt{\varepsilon_i \varepsilon_j}$) to assign LJ parameters for pairwise interactions of atoms of different type. No additional fit parameters are needed for the simulation of (non-bonded) interfaces. CHARMM-IFF reaches and can exceed DFT-level accuracy at ten million times lower computational cost.

S1.4. Simulation Protocol. Molecular dynamics simulations were carried out in the canonical ensemble (NVT) using the Nanoscale Molecular Dynamics program (NAMD)²³, as well as the Discover program in Materials Studio (mostly for short tests), using a time step of 1 fs. All atoms of the metal and of the soft matter components were allowed to move freely. The temperature was controlled at 298.15 K with the Nose-Hoover thermostat and a temperature reassignment half-life of 1 ps (Discover), or with the Langevin thermostat and a damping coefficient of 1 ps⁻¹ (NAMD). A spherical cutoff of 12 Å was applied for the summation of pair-wise Lennard-Jones interactions in high accuracy. The summation of Coulomb interactions was carried out using the Particle Mesh Ewald (PME) method with a high accuracy of 10⁻⁶ throughout the equilibration and production runs. The average temperature generally remained within ±0.15 K of the target value with instantaneous temperature fluctuations in a range of ±10 K. To accurately compute relatively small differences between large total energies of four simulation boxes and extract the adsorption energies, the average total energies of individual boxes were corrected to the exact target temperature of 298.150 K using the heat capacity of each system.

The following multi-step multi-replica protocol was employed for equilibration and conformation sampling of all particle-peptide-water systems. (1) For Pd nanoparticles, the peptides were initially positioned 2-3 nm away from the surface in vacuum and allowed to freely assemble on the particles for 1 ns before addition of water. This step was not necessary for single peptides on extended surfaces because the peptides are in immediate contact with the surface and recognize energetically favorable surface sites.

(2) Five to six independent initial configurations of all four simulation boxes were prepared for each system. A chosen system in aqueous solution was first subjected to 3 ns equilibration, followed by 2 ns production time at 298.15 K. The thermodynamic properties were recorded, including average total energies and average temperature as well as conformations of the molecules.

(3) Each individual system was annealed at 800 K for 5 ns. The coordinates of metal atoms were thereby fixed to avoid surface reconstruction and potential melting of the nanoparticle.

(4) Simulation boxes were cooled down to ambient temperature and subjected to a 5 ns period of MD simulation at room temperature allowing mobility of all atoms again. Thermodynamic data and binding configurations of peptides were analyzed to assess convergence of adsorption energies and organization of the molecules on the surface. Uncertainties of the average energies among the multiple replicas of surface-water and water-only systems were less than ± 0.6 kcal/mol and ± 0.3 kcal/mol, respectively. The small uncertainties indicate that the energies of these systems had converged. Fast energy convergence of water-only and particle-water systems is due to absence of chain molecules (peptides) with rotational degrees of freedom. The average energies of the particle-water

and water-only systems were used in all subsequent calculations of adsorption energies (equation (S1)).^{8, 20}

(5) Full equilibration, especially in the presence of multiple peptides, requires longer molecular dynamics simulations and replication of low-energy configurations to ensure energy convergence. The equilibration of single peptides in aqueous solution still yielded consistent energies of less than ± 1.0 kcal/mol uncertainty using the same protocol of 5 ns dynamics at 298 K, 5 ns at 800 K, and 5 ns at 298 K for sampling. The purpose of annealing at 800 K for 5 ns is providing an equivalent simulation time of ~ 40 ms at 298 K, or 4×10^{13} steps, according to time-temperature equivalence.²⁴ This protocol particularly aids in conformation sampling of single peptides on extended surfaces and on nanoparticle surfaces. The uncertainty in binding energy of single-peptide adsorption on extended metal surfaces was less than ± 2 kcal/mol for all peptide-surface combinations. However, conformation sampling and equilibration of multiple peptides on the Pd particles at room temperature required further extensions for convergence. The uncertainty of the computed adsorption energies after the standard 15 ns protocol was then ± 3 kcal/mol, and extensions up to 45 ns simulation time were made to explore the energy landscape that involves many barriers as follows. After completion of the general MD protocol of 5 ns at 298.15 K, 5 ns at 800 K, and 5 ns at 298.15 K, the configuration with highest average energy was discarded (least stable configuration) and two copies of the configuration of “lowest average energy” were created. These six or seven configurations were then subjected to three additional blocks of 5 ns simulation time at room temperature, allowing initial reassignment of the velocities so that molecules moved and rotated in different directions to explore new orientations and folding paths. This protocol allowed remarkable convergence of computed

adsorption energies to less than ± 1 kcal per mol peptide. In some cases, only one additional block of 5 ns simulation time was sufficient to achieve good convergence. Also completely new start conformations were employed to ascertain convergence. In summary, potential errors related to complex energy landscapes can be largely eliminated using this protocol with extensive conformation sampling, annealing, and convergence testing. This protocol is suitable for peptides of modest length (12 amino acids), which is much shorter than that of complex proteins that require more extensive experimental constraints and sampling methods.

S1.5. Relation of the Number of Adsorbed Peptides on the Particles in Experiment to the Chosen Number of Adsorbed Peptides in MD Simulations. Peptide coverage on the Pd nanoparticles under experimental conditions in solution corresponds approximately to a monolayer as suggested by QCM, NMR, and EXAFS measurements.^{2, 9, 25, 26} The number of peptides necessary to form a flat-on monolayer on the particle surface were estimated accordingly (Table S2) based on the total surface area of the nanoparticles and the average surface area per peptide (Table S3). The surface area of a spherical particle A of radius r was calculated and the maximum surface area S that each peptide can occupy on the particle surface was estimated (Table S3). Accordingly, the number of peptides in the MD simulation to achieve a monolayer coverage was chosen to be $\text{int}(\frac{A}{S}) + 1$.

For example, if 4.3 peptides was needed according to A/S , we chose 5 peptides to ensure enough peptides are available to form a monolayer on the particle surface (Table S2). The procedure lead to the same number of peptides Pd4, A6, A11, and A6,11 to represent a monolayer on the particle surfaces, even though one and two-site substitution of histidine with alanine slightly modifies the value of S . The maximum surface area S that each peptide

can approximately occupy on the surface was estimated from the molecular models in extended conformation as $S \sim 350 \text{ \AA}^2$.

S1.6. Calculation of the Adsorption Index. The adsorption index AI is a numerical measure to predict the adsorption energies of peptides on faceted nanoparticles using the weighted sum of the known adsorption energies of single peptides on extended (hkl) surfaces:

$$AI = \sum_{(hkl) \text{ facets}} w_{(hkl)} \cdot E_{ads, (hkl) surf} \quad (S3)$$

$w_{(hkl)}$ is the fraction of the (hkl) facets on the particle surface covered by the peptides, and $E_{ads, (hkl) surf}$ is the adsorption energy of a single peptide on the corresponding extended (hkl) surface. The weight factor $w_{(hkl)}$ is the product of two terms: (1) the portion of the (hkl) facet that was covered by peptide, and (2) the portion of available (hkl) facet on the particle surface.

The adsorption index provides insight into nanoparticle-specific differences in adsorption (Figure S9). However, it does not include the effect of peptide-peptide interactions, folding constraints on the nanoparticle surfaces, and effects of edges (see details in section S2).

S1.7. Analysis of the Wrapping Geometry of Nanoparticles by the Peptide Backbone. The peptide backbones are mostly in direct contact with the palladium nanoparticle surface due to strong affinity. The 12-mer peptides Pd4, A6, A11, and A6,11 are longer than the diameter of the nanoparticles with approximate end-to-end distances of 4 nm, and thus tend to wrap around the smaller nanoparticles (2-3 nm). The molecules typically bend near the intersection of surface facets to remain in close proximity to the

particle surface. To analyze the common path that the peptide backbone follows upon wrapping around the particles, we computed the probability of touching a specific (hkl) facet on the nanoparticle surface, *i.e.* (111), (110) or (100) (Figure 2 and Figure S10). Only the backbone is considered and side chains are neglected as they can cover yet a different facet and dilute the analysis of wrapping characteristics. Computation of the probability of visits to a specific facet involved the visual analysis of more than ten independent snapshots in the equilibrium state using the graphical interface of VMD.²⁷

For each particle-peptide combination, the backbone of individual peptides was selectively visualized. A specific (hkl) surface facet was marked as “visited” if any portion of the peptide backbone was positioned within 4 Å distance of the surface. Note that the chain backbone may extend over a wide area of a surface facet or it may briefly touch the surface; in either case, the facet is marked as “visited”. This protocol was then carried out for all individual peptides in a single snapshots, and it was repeated for ten other independent snapshots. The probability of a (hkl) facet visit was obtained by computing the ratio of the total instances of the (hkl) visits to the cumulative instances of “all” visits to facets.

For example, in the single snapshot shown in Figure 2a, there are 11 instances of (111) visits, 7 instances of (110) visits, and 4 instances of (100) contacts. Accordingly, the portions of (111), (110), and (100) visits are 0.5, 0.32, and 0.18, respectively. In total, for ten snapshots in the equilibrium trajectory, there are 110 instances of (111) visits, 70 instances of (110) visits, and 40 instances of (100) contacts so that the probability of (111), (110), and (100) visits remains 0.50, 0.32, and 0.18, respectively. During the course of the final production runs, the center of mass of the peptide backbone rarely moved.

Accordingly, the computed probabilities of touching a surface facet obtained from independent snapshots are almost identical and have very small uncertainty.

S1.8. Analysis of Surface Coverage and Facet Coverage by Peptides. Peptides adsorbed on the nanoparticles surface remain in nearly the same position after the simulation protocol of placement on the surface, equilibration at room temperature, and annealing at 800 K is applied (Movie S1). The analysis of facet coverage by peptides and the contribution of individual amino acids to the cumulative surface coverage was carried out using the graphical user interfaces of VMD²⁷ and Materials Studio to selectively visualize individual residues. A residue was assumed to be in direct contact with the surface if the center of mass of the residue was within 4 Å distance from the nanoparticle surface. The surface area that each residue (histidine, arginine, alanine, etc) covers on a specific facet, *i.e.* (111), (110) and (100), was computed first, and then these individual contributions were added to obtain the total coverage of specific facets (see Movies S1). For each particle-peptide arrangement, extensive visual analysis of more than ten independent snapshots of the equilibrium trajectories of lowest energy was carried out in this manner to determine the average contributions (Figures 3d, e and Figure S11). The calculation of facet and surface coverage involves all atoms of the peptides, in contrast to the analysis of the wrapping geometry of the particles where only the peptide backbone was considered. While the peptide backbone may equally likely visit (110) and (100) facets (section S1.7, Figure 2, and Figure S10), the side chains are able to preferentially cover one facet over another.

In detail, the approximate maximum surface area S_i that each residue can occupy on a flat surface was calculated first (Table S3). The surface area that each residue occupies on

the nanoparticle surface then varies between 0 (when the residue is detached from the surface) and S_i (when the residue assumes a flat-on configuration on the surface). Different residue-surface orientations other than a flat-on configuration, *e.g.*, tilted orientations and partial contacts, contribute a value of surface coverage that is smaller than S_i . To compute the surface area that a residue occupies on the surface, the surface area of that residue was projected visually onto the particle surface. Then, the projected area on a surface facet was estimated (in \AA^2) and the protocol repeated for all residues of the peptide molecules (T, S, N, A, V, H, P, R, and L) and ten other independent snapshots. Note that the contribution of multiple residues in a single chain was not distinguished separately, for example, the contributions of two leucine residues in 9th and 12th positions were reported as a single number (Figures 3d, e and Figure S11). Estimation of the projected areas onto the particle surface involved extensive visualization and pen-and-paper-like drawings using the graphical user interfaces of VMD and Materials Studio. The full analysis of more than 240 snapshots from 24 different particle-peptide combinations was very labor-intensive (>700 man-hours) and demanded extra care to minimize introduction of errors due to human judgment. The uncertainty of the computed surface coverage for individual residues was only about $\pm 0.1\%$, and the uncertainty of the total surface coverage (sum of the contributions from individual residues) about $\pm 1\%$ (Figure 3e).

Alternatively, the development of an algorithm could automate and significantly speed up the analysis of residue and peptide coverage. However, a reliable algorithm must recognize local facets on the particle surface as well as orientations of the individual amino acids including their van-der-Waals surface area to produce consistent projections. Developing such an error-free program is labor-intensive and was not pursued here.

S1.9. Computation of Reaction Rates of Peptide-Covered Particles in Stille Coupling Reactions. CHARMM-IFF was previously used to compute reaction rates of Pd nanocatalysts in hydrogenation and Stille coupling reactions.^{2,4} In hydrogenation, the rate-determining step was found to be the docking of the unsaturated compound onto exposed hydrogenated (ligand-free) Pd surface area of the particle.² For Stille coupling, atom abstraction (also called atom leaching) was found to be the rate-determining step.^{2, 4, 11} Relative reaction rates in Stille coupling for different particle morphology and size can be predicted from the bare particles, neglecting the effect of peptide coverage, in near-quantitative agreement with TOF measurements.^{2,4} The same protocol was applied here in the presence of the peptide ligands to gauge their effects on reaction rates (Figure S14).

The “abstraction energy” or “leaching energy” is the energy required to remove an individual Pd atom from the particle surface to a position which is at least 1.2 nm away from the surface. The abstraction energy of individual atoms was computed as a difference in total energy between the detached state, with the surface atom positioned away from the particle, and the bound state, with the surface atom positioned in its native position on the nanoparticle surface, using single point energies and assuming no subsequent surface reconstruction (as this would not be part of the activation energy for the reaction). The calculations were carried out using the graphical interface of Materials Studio and CHARMM-IFF resp. CVFF-IFF. For computation of the relative reaction rate, only atom types of low abstraction energies have a significant impact on reaction rate while the contributions of atom types with higher abstraction energies is negligible (if greater than $5RT \sim 3$ kcal/mol difference then the contribution is small).^{2,4}

The relative turnover frequency (TOF) in Stille coupling reactions, to enable direct comparison with experimental rate measurements, was obtained as a Boltzmann-average over the abstraction energies of all individual surface atoms N_s as previously described.⁴

The probability $P(i)$ of the detachment of an atom i is $P(i) = C \cdot e^{-\frac{E_i}{RT}}$ where C is a constant and E_i is the abstraction energy of atom i . The cumulative probability of abstraction of different surface atoms $i = 1, 2, \dots, N$ is additive due to the small magnitude of the individual probabilities (several orders of magnitude below one). Summation of the probability of the abstraction of all individual surface atoms i and normalization by the total number of Pd atoms of the particle N yields the computed relative abstraction rate R_N for a particle of a given size:

$$R_N = \frac{C}{N} \sum_{i=1}^{N_s} e^{-\frac{E_i}{RT}} \quad (\text{S4})$$

$$R_N = \frac{1}{N} \sum_{i=1}^{N_s} e^{-\frac{E_i - 50.4 \text{ kcal/mol}}{RT}} \quad (\text{S5})$$

Normalization of R_N to the total number of atoms N allows direct comparisons to measured TOFs in experiments, in which the turnover frequency is determined as the number of moles of product per unit time and per mole of catalyst (i.e. per mole Pd atoms).²⁸ Equation (S5) is equal to equation (S4) by assigning the constant C using an energy offset of 50.4 kcal/mol. The Boltzmann factors are then close to unity and numerical values of R_N scale similar to measurements to enable convenient comparisons.

The effect of peptide surface coverage of the nanoparticles on the relative reactivity was included by scaling the computed abstraction rates of bare particles in equation (S5) with an average accessibility factor a_f ($0 \leq a_f \leq 1$):

$$R_{N,SC} = \frac{a_f}{N} \sum_{i=1}^{N_s} e^{-\frac{E_i - 50.4 \text{ kcal/mol}}{RT}} \quad (\text{S6})$$

The accessibility factor a_f represents the fraction of exposed atoms available for abstraction, assuming that Pd-peptide interactions modify abstraction energies of surface atoms by a constant value for all atom, for example, $a_f \sim 0.8$. The analysis of exposure versus deactivation of surface atoms involved visualization of several snapshots in equilibrium trajectories for each peptide-particle combination and consideration of leachable atoms only (Movie S1). In equilibrium, the center of mass of the surface-adsorbed peptides typically remains in approximately the same position while the side groups show higher mobility. First, atoms of low abstraction energies were marked. Then, an atom was defined as “accessible” if it was already exposed to the solvent, or if a 1 to 2 Å displacement of small fragments would expose the atom to solvent. The ratio of exposed atoms to the total number of leachable atoms yields the accessibility factor a_f . (It is furthermore reasonable to assume that not the same reactive atoms are covered over a large interval of time due to motion of peptides on the surface). The abstraction rate of a surface covered particle $R_{N,SC}$ was then calculated according to equation (S6) where N is the total number of atoms in a nanoparticle including surface and bulk atoms, N_s is the number of atoms on the surface of a particle, E_i is abstraction energy of individual atoms on the particle surface, R is the ideal gas constant, and T the temperature (Figure S14).

S1.10. Synthesis of Peptide-Capped Pd Nanoparticles, and Analysis of Particle Size Using TEM. Peptide-capped Pd nanoparticles were synthesized with A10, A6,10, A10,11 and A6,10,11 peptides (Peptide 2.0) using previously established methods.²⁹ Scanning transmission electron microscopy (STEM) imaging for size analysis was

performed on a spherical aberration corrected JEOL-ARM 200F operating at an accelerating voltage of 200 kV. The microscope was operated in scanning mode and all images shown are annular dark field (ADF) STEM images. The detector inner collection angle for HAADF imaging was ≈ 70 mrad; high resolution imaging was performed with a spot size of 8c and pixel dwell time of 25 μ s. Samples were prepared on ultrathin carbon TEM grids (Ted Pella, USA) by drop casting 5 μ L of nanoparticles diluted by a factor of 50 onto the grid and drying them in air. Prior to high resolution imaging the samples were cleaned for 45 seconds in a 97% H₂, 3% O₂ plasma to remove hydrocarbon contaminants (Fischione model 1070). Mean particle sizes for each sample were determined from size measurements of at least 150 nanoparticles from at least 4 different images. Nanoparticle sizes were measured using ImageJ.

S2. Interpretation and Limitations of the Adsorption Index

The adsorption index AI estimates the adsorption energies of multiple peptides on faceted nanoparticles using the “ideal” input from the adsorption energies of single peptides on flat (111), (100), and (110) surfaces. It uses the known adsorption energies of the peptides on extended (hkl) surfaces $E_{ads,(hkl) surf}$ and the fraction of the (hkl) facets on the particle surface $w_{(hkl)}$ as a weight factor in a summation according to equation (S3) (Figure S9).

On the other hand, the exact adsorption energies of a monolayer of peptides on the particles E_{ads} , normalized by the number of peptides N , can be seen to represent the attraction of an isolated peptides plus “corrections“ for the competition among multiple peptides and for conformation restrictions due to specifically folded states.

The computed AI illustrates a clear trend among particles of different sizes (Figure S9). The magnitude of the Adsorption Index of peptides is greater toward larger particles which indicates the peptides have fewer challenges to adapt their conformation on the particle surface. The difference between true computed adsorption energies (Figure 1) and the adsorption index AI (Figure S9) reveals that the energy cost associated with adjustment to a folded conformation on the particle surface (in contrast to extended configuration on flat surfaces) as well as the competition of multiple peptides for direct adsorption on nanoparticle surface is around +10 to +15 kcal/mol.

The adsorption index therefore provides an intuitive estimate of the adsorption energy yet also suffers from the following limitations. (1) Intermolecular interactions between several peptide molecules on the particle surface are neglected (which can be positive or negative), (2) high surface curvature of small 2 to 3 nm particles and challenges related to conformational adaptation of the chain molecules are neglected, (3) modified attraction of

peptides near the edges of the nanoparticles is not taken into account,³ and (4) competitive adsorption of peptides as well as limited availability of attractive surface facets such as (111) and (110) complicate straightforward prediction of adsorption energies.^{3, 30, 31} Adsorption tends to be stronger on larger particles, closer to the estimate by the adsorption index, as surface crystal facets are well-defined. Adsorbed molecules then also have fewer conformational constraints.

The impact of particular peptide-peptide interactions on facet preferences as a function of peptide concentration can be analyzed by simulations (or experiments) by changing the number of the adsorbed peptides.^{3, 25}

The adsorption index is similar to an additive estimate of the adsorption energy of oligomeric peptides on even (111) surfaces from known adsorption energies of single amino acids.²⁰ The qualitative trend from additive estimates was also consistent with computed adsorption energies for a series of peptides, although significantly larger (further below zero) than adsorption energies due to neglect of folding specifics of the peptide.

S3. Additional Tests of Particle Size Using R→A Mutants

To further validate the relationships between amino acid sequence, surface coverage, and particle size, four additional mutants of peptide Pd4 were synthesized and tested in nanoparticle growth (Table S1). R was substituted by A and led to smaller nanoparticles compared to the H→A substituted nanoparticles (Figure S13). The introduction of A likely increased the conformational flexibility of the peptides and the surface coverage on nascent nanoparticles so that the peptides could arrest particle growth sooner (Figure S13a-f). Particularly on small nanoparticles below 1.5 nm size, the planar and stiff guanidinium group in R of nearly 0.7 nm size cannot interact effectively with the surface, even though

it is among the strongest binders to flat (111) surfaces.¹⁴ At the same time, the introduction of multiple A residues such in the A6,10,11 peptides weakens binding as A is a conformationally flexible yet weakly binding residue.¹⁴ Several larger, agglomerated nanoparticles are then observed in the size distribution, partly above 4 nm (Figure S13g, h). Also the dialanine peptides exhibit a notable fraction of larger nanoparticles (Figure S13c-f). Accordingly, high R content is not favorable for the early stabilization of emerging nanoparticles yet R and H are among the strongest binding residues for larger nanoparticles and extended (111) surfaces.¹⁴ Therefore, mutants entirely without R and H such as A6,10,11 peptides do not reach sufficient binding strength beyond a certain threshold size and result in poor shape and size control.

S4. Tests of Catalytic Activity

The specific surface environments become of practical interest in catalysis. Differences in reactivity across orders of magnitude have been observed, for example, in Stille coupling reactions. Prior computational predictions of relative reaction rates using CHARMM-IFF are in good agreement with turnover frequency (TOF) measurements for the same systems.^{2,9,25,28,29} Mechanistically, the abstraction of superficial Pd atoms by an aryl halide (Ar-X) is the rate-determining step^{4, 11} and the computation of the relative reaction rate involves a Boltzmann average over the abstraction energy of all surface-accessible Pd atoms (see details in section S1.9).^{2,4,11} Here, we computed the reaction rates for the ideal, near-spherical nanoparticles again, in the presence and in the absence (under neglect) of the peptide ligands. It is found that only the highlighted Pd atoms of low abstraction energy make a significant contribution to the reaction (Figure S14a), and that the ligands lower

the reaction rate consistently by ~20% for various nanoparticles sizes and bound peptides (Figure S14b).

Therefore, the peptide ligands block some active sites on the surface, although the fraction of available undercoordinated reactive sites remains high at about 80% (Movie S1). Nanoparticles of different size and with different peptide ligands lead to similar surface accessibility so that the reduction in relative abstraction rates and reactivity is about the same (Figure S14b). Overall, the difference in reactivity between the ligand covered nanoparticles and the bare nanoparticles is small. Good agreement with experimental measurements can become more quantitative by taking into account exact nanoparticle structures and polydispersity from HE-XRD data as previously reported in ref. ². The main focus and conclusion in this work is that comparatively large peptide ligands in relation to the size of the resulting near-spherical nanoparticles play an essential role in growing a tailored catalyst. The peptide ligands exert influences on particle growth, size, as well as very specific local surface features and surface disorder that can greatly enhance the reactivity. The impact of the actual ligands on the catalytic reactivity, after the particles are grown, can vary, for example, from minor for Stille coupling to detrimental for hydrogenation reactions.

Supporting References

1. A. Gupta, B. Boekfa, H. Sakurai, M. Ehara and U. D. Priyakumar, *J. Phys. Chem. C*, 2016, **120**, 17454-17464.
2. N. M. Bedford, H. Ramezani-Dakhel, J. M. Slocik, B. D. Briggs, Y. Ren, A. I. Frenkel, V. Petkov, H. Heinz, R. R. Naik and M. R. Knecht, *Acs Nano*, 2015, **9**, 5082-5092.
3. H. Ramezani-Dakhel, L. Y. Ruan, Y. Huang and H. Heinz, *Adv. Funct. Mater.* , 2015, **25**, 1374-1384.
4. H. Ramezani-Dakhel, P. A. Mirau, R. R. Naik, M. R. Knecht and H. Heinz, *Phys. Chem. Chem. Phys.*, 2013, **15**, 5488-5492.
5. *Journal*, 2006.
6. *Accelrys Inc., San Diego, CA*, 2011.
7. D. R. Lide, ed., *CRC Handbook of Chemistry and Physics* CRC Press, Boca Raton, FL, 2015.
8. H. Heinz, *J. Comput. Chem.*, 2010, **31**, 1564-1568.
9. R. Coppage, J. M. Slocik, B. D. Briggs, A. I. Frenkel, R. R. Naik and M. R. Knecht, *Acs Nano*, 2012, **6**, 1625-1636.
10. R. Coppage, J. M. Slocik, H. Ramezani-Dakhel, N. M. Bedford, H. Heinz, R. R. Naik and M. R. Knecht, *J. Am. Chem. Soc.*, 2013, **135**, 11048-11054.
11. B. Briggs, N. Bedford, S. Seifert, H. Koerner, H. Ramezani-Dakhel, H. Heinz, R. R. Naik, A. Frenkel and M. R. Knecht, *Chem. Sci.*, 2015, **6**, 6413-6419.
12. C. Y. Chiu, Y. J. Li, L. Y. Ruan, X. C. Ye, C. B. Murray and Y. Huang, *Nature Chem.*, 2011, **3**, 393-399.

13. L. Ruan, H. Ramezani-Dakhel, C.-Y. Chiu, E. Zhu, Y. Li, H. Heinz and Y. Huang, *Nano Lett.*, 2013, **13**, 840-846.
14. J. Feng, R. B. Pandey, R. J. Berry, B. L. Farmer, R. R. Naik and H. Heinz, *Soft Matter*, 2011, **7**, 2113-2120.
15. H. Heinz, T.-J. Lin, R. K. Mishra and F. S. Emami, *Langmuir*, 2013, **29**, 1754-1765.
16. H. Heinz and H. Ramezani-Dakhel, *Chem. Soc. Rev.*, 2016, **45**, 412-448.
17. A. D. MacKerell, Jr., D. Bashford, M. Bellott, R. L. Dunbrack, Jr., J. D. Evanseck, M. J. Fields, S. Fischer, J. Gao, H. Guo, S. Ha, D. Joseph-McCarthy, L. Kuchnir, K. Kuczera, F. T. K. Lau, C. Mattos, S. Michnick, T. Ngo, D. T. Nguyen, B. Prodhom, W. E. Reiher, III, B. Roux, M. Schlenkrich, J. C. Smith, R. Stote, J. Straub, D. Watanabe, J. Wiórkiewicz-Kuczera, D. Yin and M. Karplus, *J. Phys. Chem. B*, 1998, **102**, 3586-3616.
18. H. Heinz, R. A. Vaia, B. L. Farmer and R. R. Naik, *J. Phys. Chem. C*, 2008, **112**, 17281-17290.
19. H. Heinz, B. L. Farmer, R. B. Pandey, J. M. Slocik, S. S. Patnaik, R. Pachter and R. R. Naik, *J. Am. Chem. Soc.*, 2009, **131**, 9704-9714.
20. J. Feng, J. M. Slocik, M. Sarikaya, R. R. Naik, B. L. Farmer and H. Heinz, *Small*, 2012, **8**, 1049-1059.
21. N. E. Singh-Miller and N. Marzari, *Phys. Rev. B*, 2009, **80**, 235407.
22. M. P. Allen and D. J. Tildesley, *Computer Simulation of Liquids*, Clarendon Press, Oxford, 1987.
23. J. C. Phillips, R. Braun, W. Wang, J. Gumbart, E. Tajkhorshid, E. Villa, C. Chipot, R. D. Skeel, L. Kale and K. Schulten, *J. Comput. Chem.*, 2005, **26**, 1781-1802.

24. K. C. Jha, H. Liu, M. R. Bockstaller and H. Heinz, *J. Phys. Chem. C*, 2013, **117**, 25969-25981.
25. R. Coppage, J. M. Slocik, B. D. Briggs, A. I. Frenkel, H. Heinz, R. R. Naik and M. R. Knecht, *J. Am. Chem. Soc.*, 2011, **133**, 12346-12349.
26. D. B. Pacardo, J. M. Slocik, K. C. Kirk, R. R. Naik and M. R. Knecht, *Nanoscale*, 2011, **3**, 2194-2201.
27. W. Humphrey, A. Dalke and K. Schulten, *J. Mol. Graphics*, 1996, **14**, 33-38.
28. R. Coppage, J. M. Slocik, M. Sethi, D. B. Pacardo, R. R. Naik and M. R. Knecht, *Angew. Chem.-Int. Edit.*, 2010, **49**, 3767-3770.
29. D. B. Pacardo, M. Sethi, S. E. Jones, R. R. Naik and M. R. Knecht, *Acs Nano*, 2009, **3**, 1288-1296.
30. T. Moldt, D. Brete, D. Przyrembel, S. Das, J. R. Goldman, P. K. Kundu, C. Gahl, R. Klajn and M. Weinelet, *Langmuir*, 2015, **31**, 1048-1057.
31. D. Costa, L. Savio and C. M. Pradier, *Journal of Physical Chemistry B*, 2016, **120**, 7039-7052.